Morphology, photometry and kinematics of N-body bars. I Three models with different halo central concentrations

E. Athanassoula, A. Misiriotis

Mon. Not. R. Astron. Soc. **330,** 35–52 (2002)

Morphology, photometry and kinematics of *N*-body bars – I. Three models with different halo central concentrations

E. Athanassoula[1]★ and A. Misiriotis[1,2]

[1]*Observatoire de Marseille, 2 Place Le Verrier, F-13248 Marseille Cedex 4, France*
[2]*University of Crete, Physics Department, PO Box 2208, 710 03 Heraklion, Crete, Greece*

Accepted 2001 October 8. Received 2001 July 23

ABSTRACT

We discuss the morphology, photometry and kinematics of the bars which have formed in three *N*-body simulations. These have initially the same disc and the same halo-to-disc mass ratio, but their haloes have very different central concentrations. The third model includes a bulge. The bar in the model with the centrally concentrated halo (model MH) is much stronger, longer and thinner than the bar in the model with the less centrally concentrated halo (model MD). Its shape, when viewed side-on, evolves from boxy to peanut and then to 'X'-shaped, as opposed to that of model MD, which stays boxy. The projected density profiles obtained from cuts along the bar major axis, for both the face-on and the edge-on views, show a flat part, as opposed to those of model MD which are falling rapidly. A Fourier analysis of the face-on density distribution of model MH shows very large $m = 2, 4, 6$ and 8 components. Contrary to this, for model MD the components $m = 6$ and 8 are negligible. The velocity field of model MH shows strong deviations from axial symmetry, and in particular has wavy isovelocities near the end of the bar when viewed along the bar minor axis. When viewed edge-on, it shows cylindrical rotation, which the MD model does not. The properties of the bar of the model with a bulge and a non-centrally concentrated halo (MDB) are intermediate between those of the bars of the other two models. All three models exhibit a lot of inflow of the disc material during their evolution, so that by the end of the simulations the disc dominates over the halo in the inner parts, even for model MH, for which the halo and disc contributions were initially comparable in that region.

Key words: methods: numerical – galaxies: kinematics and dynamics – galaxies: photometry – galaxies: structure.

1 INTRODUCTION

A bar is an elongated concentration of matter in the central parts of a disc galaxy. Within this loose and somewhat vague definition fit a number of very different objects. Thus, different bars have very different masses, axial ratios, shapes, mass and colour distributions. They can also have widely different kinematics. Several observational studies have been devoted to the structural properties of bars and/or to their morphology, photometry and kinematics, thus providing valuable information on these objects and on their properties.

Many *N*-body simulations of the evolution of disc galaxies have witnessed the formation of bars. Most studies have focused on understanding what favours or hinders bar formation. Not much work, however, has been done on the 'observable' properties of *N*-body bars. This is quite unfortunate because such studies are necessary for the comparison of real and numerical bars. In fact, several observational studies have taken an *N*-body simulation available in the literature and have analysed it in a way similar to that used for the observations in order to make comparisons (e.g. Kormendy 1983; Ohta, Hamabe & Wakamatsu 1990; Lütticke, Dettmar & Pohlen 2000). Although this is very useful, it suffers from lack of generality, as the specific simulation may not be appropriate for the observational question at hand, and as it does not give a sufficient overview of the alternative properties *N*-body bars can have. Here we will approach the comparisons between real and *N*-body bars from the simulation side, giving as wide a range of alternatives as possible, while making an analysis as near as possible to that used by observers. We hope that in this way our work will be of use to future observational studies and will provide results for detailed comparisons.

An obvious problem when comparing *N*-body bars to real bars is that simulations trace mass, while observations give information on the distribution of light. The usual way to overcome this hurdle is to assume a constant *M*/*L* ratio. This assumption should be adequate for the inner parts of galaxies (e.g. Kent 1986; Peletier &

★E-mail: lia@paxi.cnrs-mrs.fr

Balcells 1996), particularly early types that have relatively little star formation, and in the near-infrared wavelengths, where the absorption from dust is least pronounced.

By their nature, real bars can be observed in only a much more limited way than *N*-body bars. Galaxies are projected on the plane of the sky and their deprojection is not unambiguous, particularly for barred galaxies, which are the object of the present study. This problem of course does not exist for simulations, which we furthermore can 'observe' from any angle we wish. It is thus possible to 'observe' the same snapshot both face-on and edge-on. This is of course impossible to do for real galaxies and has led to a number of complications, e.g. regarding the nature of peanuts and the 3D structure of bars. A second limitation is that in observations light is integrated along the line of sight and one cannot observe the various components separately, as in *N*-body bars. Finally, the biggest limitation comes from the fact that there is no direct way to observe dark matter, while in *N*-body simulations the halo can be analysed as any other component of the galaxy. All these limitations lead to complications in the comparisons, but are also one of the reasons as to why the observations of *N*-body bars are most useful. We can observe our bars both in the restricted manner that real galaxies allow and in the more detailed manner accessible to simulations and, by comparing the two, derive the signatures of the latter in the former. This can help us obtain information on properties of real bars which are not directly observable.

In this paper we will discuss at length the observable properties of three simulations. In Section 2 we present the simulations and their initial conditions. In Section 3 we present the basic properties of our three fiducial models and in Section 4 we present the shape and the axial ratio of the isodensities in the bar region. Projected density profiles with the disc seen face-on and edge-on are presented in Sections 5 and 6, respectively. In Section 7 we present the Fourier components of the mass distribution seen face-on, in Section 8 we compare various ways of measuring the bar length, and in Section 9 we quantify the peanut shape. Kinematics are presented in Sections 10 and 11 and the shape of the bulge is discussed in Section 12. We summarize in Section 13. In a companion paper (Athanassoula, in preparation, hereafter Paper II) will present more simulations, compare them to observations and discuss implications about the distribution of the dark matter in barred galaxies.

In this paper and its companion we will willingly refrain from discussing resonances, their location and their effect on the evolution of the bar. This discussion necessarily implies the knowledge of the pattern speed of the bar, which is not directly available from observations. Together with the discussions relying on dynamics and/or some knowledge of the orbital structure, issues implying resonances will be left for a future paper.

2 SIMULATIONS

We have made a large number of simulations of bar-unstable discs, three of which we will discuss in this paper. Each is characteristic of a class of models, other members of which will be discussed in Paper II.

In order to prepare the initial conditions we basically followed the method of Hernquist (1993), to which we brought a few improvements, described in Appendix A.

The density distribution of the disc is given by

$$\rho_{\rm d}(R,z) = \frac{M_{\rm d}}{4\pi h^2 z_0}\exp(-R/h)\,\mathrm{sec}\,h^2\left(\frac{z}{z_0}\right), \tag{1}$$

that of the bulge by

$$\rho_{\rm b}(r) = \frac{M_{\rm b}}{2\pi a^2}\frac{1}{r(1+r/a)^3}, \tag{2}$$

and that of the halo by

$$\rho_{\rm h}(r) = \frac{M_{\rm h}}{2\pi^{3/2}}\frac{\alpha}{r_{\rm c}}\frac{\exp(-r^2/r_{\rm c}^2)}{r^2+\gamma^2}. \tag{3}$$

In the above, r is the radius, R is the cylindrical radius, $M_{\rm d}$, $M_{\rm b}$ and $M_{\rm h}$ are the masses of the disc, bulge and halo respectively, h is the disc radial scalelength, z_0 is the vertical scale thickness of the disc, a is the scalelength of the bulge, and γ and $r_{\rm c}$ are scalelengths of the halo. The parameter α in the halo density equation is a normalization constant defined by

$$\alpha = \{1-\sqrt{\pi}\exp(q^2)[1-\mathrm{erf}(q)]\}^{-1}, \tag{4}$$

where $q = \gamma/r_{\rm c}$ (cf. Hernquist 1993). In all simulations we have taken $M_{\rm d} = 1$, $h = 1$ and have represented the disc with 200 000 particles. The halo mass, calculated to infinity, is taken equal to 5, and $r_{\rm c}$ is always taken equal to 10. The halo mass distribution is truncated at 15. The disc distribution is cut vertically at $z_{\rm cut} = 3z_0$ and radially at half the halo truncation radius, i.e. $R_{\rm cut} = 7.5$. The velocity distributions are as described by Hernquist (1993) and in Appendix A.

The first two fiducial models that we will discuss at length here have very different central concentrations. For the first one we have taken $\gamma = 0.5$, so that the halo is centrally concentrated and in the inner parts has a contribution somewhat larger than that of the disc. As the mass of the disc particles is the same as that of the halo particles, the number of particles in the halo is set by the mass of the halo within the truncation radius (in this case, roughly 4.8) and in this simulation is roughly equal to 963 030. We will hereafter call this model the 'massive halo' model, or, for short, MH. For the second model we have taken $\gamma = 5$, so that the disc dominates in the inner parts. The halo is represented by 931 206 particles. We will hereafter call this model the 'massive disc' model, or, for short, MD. Both the MH and MD models have no bulge. In order to examine the effect of the bulge, we will consider a third fiducial model, which is similar to MD but has a bulge of mass $M_{\rm b} = 0.6$ and of scalelength $a = 0.4$. We will hereafter refer to this model as the 'massive disc with bulge', or, for short, MDB. In the three fiducial simulations we adopted a disc thickness of $z_0 = 0.2$ and $Q = 0.9$. Their circular velocity curves are shown in Fig. 1, together with the contribution of each component separately. For model MDB we also show the total contribution from the two spherical components. The halo and disc contributions in the inner parts are comparable in the case of model MH, while the disc dominates in model MD. For model MDB, as one moves from the centre outwards one has first a bulge-dominated part, then a disc-dominated part and finally a halo-dominated part. Thus its evolution could in principle be different from both that of the MH and that of the MD models. All three cases have a flat rotation curve, at least within a radius of five disc scalelengths. If we consider larger radii, say up to 15 disc scalelengths, then the rotation curves for models MD and MDB are still flat, whereas that of model MH decreases, because its halo is centrally concentrated. By adding an extra extended halo component, we can keep the rotation curve flat up to such distances. This, however, more than doubles the total mass of the system and raises the number of particles accordingly, to a number which was beyond our CPU capacities, particularly because of the large number of MH-type

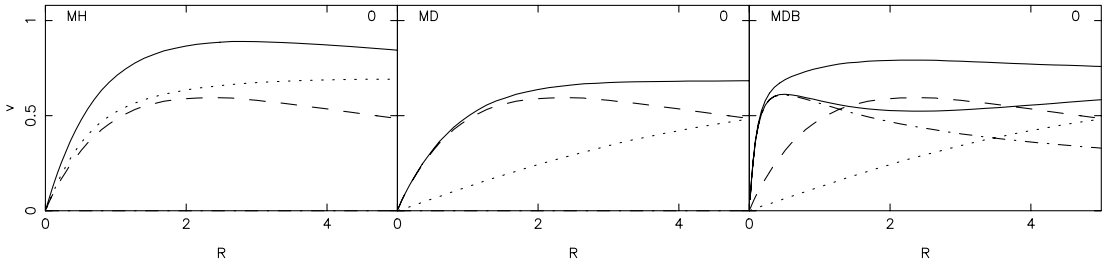

Figure 1. Circular velocity curves of our three fiducial models at the beginning of the simulation. The dashed, dotted and dash-dotted lines give the contributions of the disc, halo and bulge respectively, while the thick full lines give the total circular velocity curves. For simulation MDB we also give the total contribution from the two spherical components with a thin solid line. The left-hand panel corresponds to simulation MH, the middle one to simulation MD and the right-hand one to simulation MDB. The simulation name is given in the upper left-hand corner and the time in the upper right-hand corner of each panel.

simulations described in this and the companion paper. We thus ran a simulation with particles of double the mass, and therefore half the number. This allowed us to check that the introduction of this extended halo does not change qualitatively the results of the morphology, photometry and kinematics of the bar. Having established this, and because this simulation has only 100 000 particles in the disc, so that the noise is higher and the quantities describing the bar which are discussed here less well defined, we will present in this paper the results of the simulation without the more extended halo component.

These three simulations are part of a bigger ensemble, covering a large fraction of the available parameter space. In this paper we will discuss only these three, which are each characteristic of a certain type of simulation. By limiting ourselves to three simulations, we will be able to make a very thorough analysis of each case. In Paper II we will discuss more simulations in order to assess how certain parameters, such as Q or the thickness of the disc, influence the main results presented here.

The simulations were carried out on a Marseille Observatory GRAPE-5 system consisting of two GRAPE-5 cards (Kawai et al. 2000) coupled via a PCI interface (Kawai et al. 1997) to a Compaq DS 20 or an XP-1000. We used a GRAPE treecode similar to that initially built for the GRAPE-3 system (see e.g. Athanassoula et al. 1998). For simulation MH we used an opening angle of 0.7, while for simulations MD and MDB we used an opening angle of 0.6. With the XP-1000 front end, one time-step for 10^6 particles takes roughly 15 s for $\theta = 0.6$ and less than 12 s for $\theta = 0.7$. We used a softening of 0.0625 and a time-step of 0.015 625. This gave us an energy conservation better than or of the order of one part in a thousand over the entire simulations, which were terminated after $t = 900$, i.e. after 57 600 time-steps. Full information on all the particles in the simulation is kept every 20 time units, while information on the total potential and kinetic energy and on the centre of mass of the system is saved every 8 time-steps, i.e. every 0.125 time units. We calculate on line (Athanassoula et al. 1998) the amplitude and the phase of the $m = 2$ and 4 Fourier components of the mass every 0.5 time units. We also produce GIF files of the face-on and edge-on distributions of the disc particles every 0.5 time units which, when viewed consecutively as a movie with the help of the XANIM software, give a good global view of the evolution.

In this paper, unless otherwise noted, all quantities are given in computer units scaled so that the scalelength of the disc is unity, the total mass of the disc equal to 1 and $G = 1$. It is easy to convert them to standard astronomical units by assigning a mass and a scalelength to the disc. Thus, if the mass of the disc is taken to be equal to $5 \times 10^{10}\,\mathrm{M}_\odot$ and its scalelength equal to 3.5 kpc, we find that the unit of mass is $5 \times 10^{10}\,\mathrm{M}_\odot$, the unit of length is 3.5 kpc, the unit of velocity is $248\,\mathrm{km\,s^{-1}}$ and the unit of time is 1.4×10^7 yr. Thus time 500 corresponds to 7×10^9 yr and time 800 to 1.1×10^{10} yr. This calibration, however, is not unique. Adopting different values for the disc scalelength and mass would have led to alternative calibrations.

3 TWO TYPES OF *N*-BODY BARS

Figs 2 and 3 give some basic information on the three fiducial simulations at times 600 and 800 respectively. The upper panels give the total circular velocity curves, together with the contribution of each component separately. In all three cases the disc material has moved inwards as a result of the evolution and the configurations become much more centrally concentrated. As a result, the circular velocity curve of model MH rises much faster than initially and after the rising part stays roughly constant. Also the centre-most part is disc dominated, contrary to what was the case at the start of the simulation. The circular velocity curves of models MD and MDB develop a peak near the centre, also due to the increased central concentration of the disc material. In model MD all the central part is disc-dominated, as it was at the start of the simulation. On the other hand, for model MDB there is no region which is disc-dominated because of the joint effect of the halo and bulge. There is not much difference between the circular velocity curves at times 600 and 800.

Observed face-on[1] (second and fifth rows in Figs 2 and 3) the disc particle distributions are quite different in the three fiducial cases. The bar in the MH model is longer and thinner than the bar in model MD. At time $t = 600$ it has 'ansae' at the extremities of the bar, similar to those observed in early type barred galaxies. These structures do not exist at time 800. The bar in model MD is rather short and fat, while the bar in model MDB is intermediate both in length and shape of the bars of models MD and MH, but nearer to that of MH.

Model MH has a ring, which observers would call an inner ring as it surrounds the bar and its radius is roughly equal to the semi-major axis of the bar. It shows up clearer in the dot-plots of the fifth row than in the isodensity plots of the second row. It can be discerned in the isodensity plots at time 800, but not at time 600, because of the fact that the region between the ring and the bar has a much lower projected surface density at the later time. Such a ring does not exist in the MD model. For model MDB it shows as a broad diffuse structure. In model MH the ring has a density enhancement near the ends of the bar both at times 600 and 800,

[1] Unless otherwise noted, in this paper we adopt a coordinate system such that the x and y axes lie on the equatorial plane, the y axis being along the bar major axis.

which is slightly stronger towards the leading side. In fact, rings have not been witnessed before now in purely stellar *N*-body simulations, with the notable exception of the fiducial simulation of Debattista & Sellwood (2000). It is worth noting that both in their simulation and in our MH model the maximum of the halo rotation curve is near the centre of the galaxy.

We use the methods described in Appendix B to determine the parameters of the ring. Applying the local (global) method to model MH at time $t = 600$, we find that the ring has a radius of 3.0 (3.2) and an axial ratio b/a of 0.7 (0.8). It is very thick – the width of the fitting Gaussian (cf. Appendix B) being of the order of 1.8 (1.4) –, it is aligned parallel to the bar major axis and its mass is 31 (28) per cent of the total disc mass. For time $t = 800$ we find that the radius is 3.6 (3.7) and the axial ratio 0.8 (0.9). The width of the

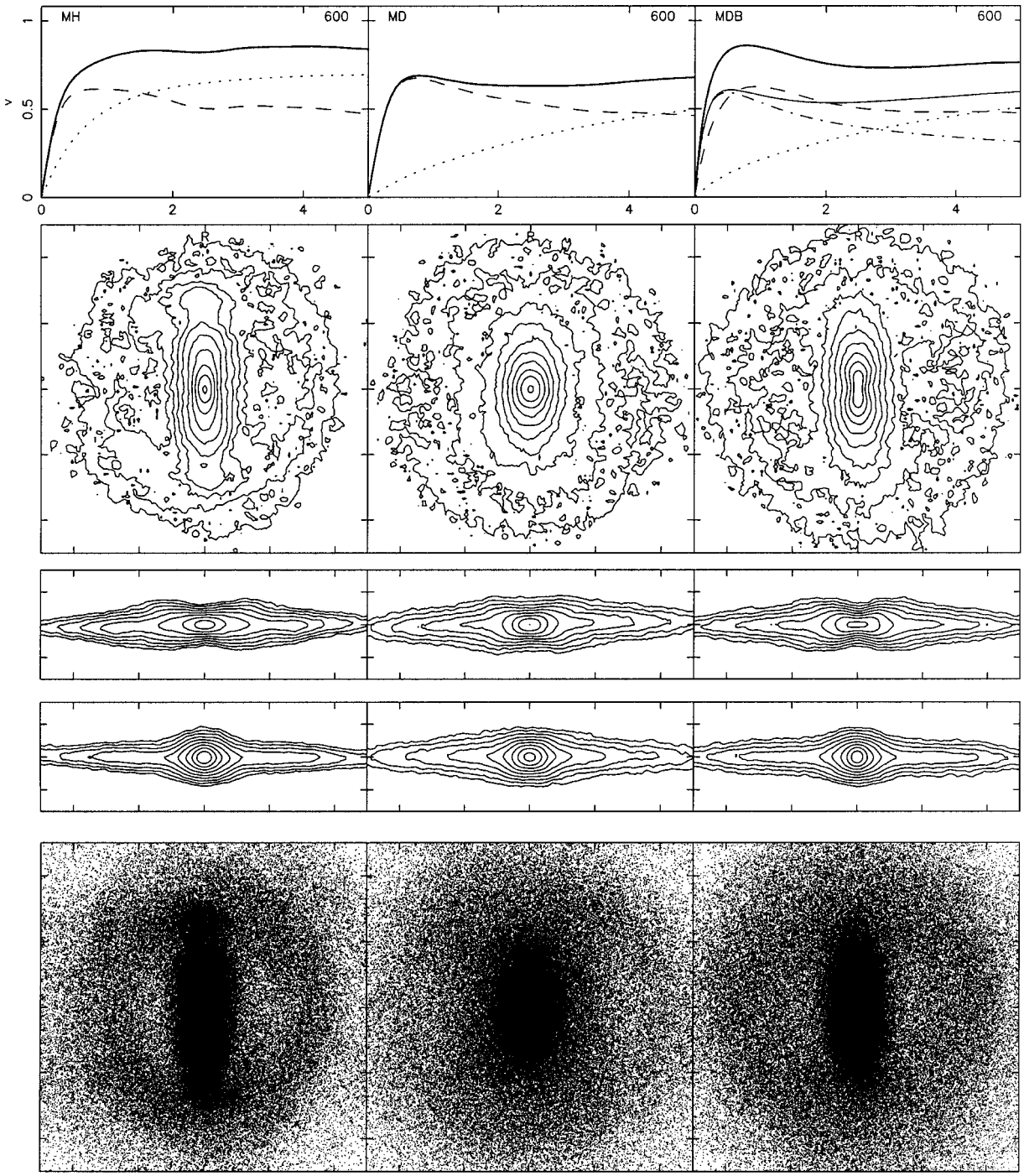

Figure 2. Basic information on the three fiducial simulations at time $t = 600$. Left-hand panels correspond to simulation MH, middle panels to simulation MD and right-hand panels to simulation MDB. The upper panels give the circular velocity curve. The dashed, dotted and dash-dotted lines give the contributions of the disc, halo and bulge, respectively, while the thick full lines give the total circular velocity curves. For simulation MDB we also give the total contribution from the two spherical components (thin solid line). The second row of panels gives the isocontours of the density of the disc particles projected face-on, and the third and fourth rows the side-on and end-on edge-on views, respectively. The fifth row of panels gives the dot-plots of the particles in the (x, y) plane. The side of the box for the face-on views is 10 units, and the height of the box for the edge-on views is 3.33 units.

fitting Gaussian is 1.4 (1.3), it is aligned parallel to the major axis of the bar and its mass is 20 (20) per cent of the total disc mass. This shows that the ring has become less eccentric and that its diameter has increased with time. The results from the two methods agree well, but they both overestimate the mass of the ring, because they consider the total mass under the fitted Gaussian, so that the wings of the Gaussian contribute substantially. Had we truncated the Gaussian we would have obtained a considerably lower value. Because, however, we do not know where to truncate it, we leave it as it is, and let the reader obtain the mass after truncation from the values of the parameters we give above.

Model MDB also shows a ring. At times 600 its radius is 3.1 (3.2) and its axial ratio is 0.9 (0.9). It is even broader than the ring in model MH – the width of the Gaussian being of the order of 2.1 (1.9) – and thus we can not give a reliable estimate of its mass, as argued in Appendix B. At times 800 its radius is 3.6 (3.6) and its shape is near-circular. Again we note that the size of the ring has increased with time and that its shape has become more circular. Again there is good agreement between the two methods.

The edge-on projections of the disc density (given by isodensities in the third and fourth rows in Figs 2 and 3) are also

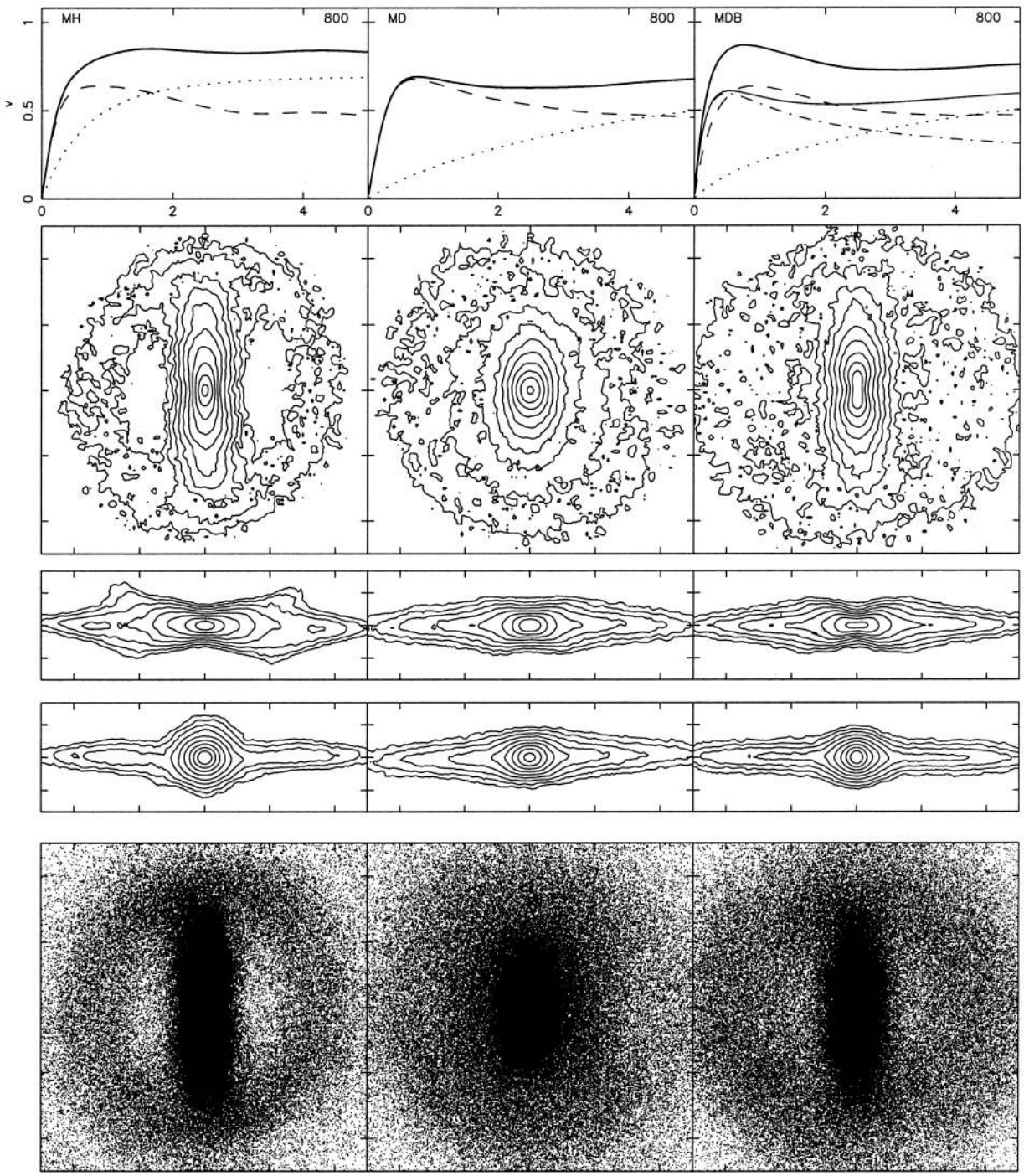

Figure 3. Same as for Fig. 2, but for time $t = 800$.

widely different in the three fiducial cases. In the side-on[2] view, model MD has a boxy outline. On the other hand model MH is peanut-like at time 600 and is 'X'-shaped at time 800. Model MDB has the form of a peanut. Seen end-on, models MH and MDB show a central structure of considerable size, which could well be mistaken for a bulge. This is particularly strong for model MH at time 800. At that time we also see the signature of the ring on the side-on view, as closing isodensities on either side of the central area.

4 THE AXIAL RATIO AND SHAPE OF THE ISODENSITIES IN THE BAR REGION: FACE-ON VIEW

In order to measure the axial ratio and shape of the bar isodensities seen face-on we project all disc particles on the (x, y) plane on which we superpose a 200×200 Cartesian grid covering a square of length $(-16, 16)$. The density at the centre of each cell is calculated by counting the number of particles in the cell and dividing by its area. The density at intermediate points is calculated using bilinear interpolation. We then fit generalized ellipses to the isodensities. The equation of the generalized ellipse, initially introduced by Athanassoula et al. (1990), is

$$(|x|/a)^c + (|y|/b)^c = 1, \tag{5}$$

where a and b are the semi-major and semi-minor axes respectively, and c is a parameter describing the shape of the generalized ellipse. For $c = 2$ we obtain a standard ellipse, for $c < 2$ a lozenge, while for $c > 2$ the shape approaches a rectangle, and will, for simplicity, be called hereafter rectangular-like. Athanassoula et al. (1990) have used generalized ellipses to quantify the shape of the isophotes of strongly barred early-type galaxies and we will use them here to describe the shape of our *N*-body bars. Unfortunately the comparison between the two is not as straightforward as it sounds. All galaxies in the Athanassoula et al. sample have a sizeable bulge, so that it was not possible to get information on the isophotes of the inner parts of the bar. Because isophotes are determined both by the light of the bulge and that of the bar, it was necessary to blank out the inner parts of the galaxy, where the bulge light dominates. In a few cases there were also small spiral features starting off from the end of the bar, and these also had to be blanked out. As the sample was relatively small it was possible to determine interactively the areas to be blanked out, separately in each frame.

Models MH and MD have no bulge, so it is possible to continue the fits much further in than in the case of early-type barred galaxies. (It is nevertheless recommended to exclude the innermost few pixels, where the shape of the pixel may influence the shape of the isophote). Comparisons with observations, however, will not extend all the way to the centre. Model MDB has a sizeable bulge, but we fitted the generalized ellipses to the disc component only. We did this in order to be able to discuss the effect of the bulge on the real shape of the bar, rather than the shape of the disc and bulge components combined. This is trivial to do in the case of models, but of course impossible for real galaxies. We will discuss at the end of this Section how the existence of the bulge obscures the issue when the generalized ellipses are fitted to both components, as is the case in real galaxies.

[2] We call the edge-on view for which the line of sight is along the minor axis of the bar the side-on view. Similarly we call the edge-on view where the line of sight is along the major axis of the bar the end-on view.

For every simulation and for every time-step for which full information on the particle positions is available – i.e. 45 time-steps per simulation – we fitted generalized ellipses to 70 isodensities covering the density range in the disc. We repeated the exercise twice, once generously excluding a central region, and the other excluding only a very small central region. For reasons of homogeneity, and considering the very large number of frames to be treated, we determined the area to be blanked out automatically and not interactively. For this we first took the difference of the projected density along the minor and major axes of the bar and calculated the radius at which this is maximum. In the first passage we excluded all the region within this radius, and in the second the region within one tenth of this radius. We made several tests with other blanking radii and thus asserted that our results are not dependent on this radius. Because the blanking out was done automatically we did not blank out the spirals coming from the ends of the bar. This presents problems in the early steps of the simulations, where the spirals are important and therefore influence wrongly the fits. In the later stages though, no such spirals are present, and the fits pertain to the bar only.

For model MD the generalized ellipses fit the isodensities very well all the way to the centre, and thus the results obtained with the generous and those obtained with the limited blanking agree very well in the region where both give information. This is true also for most of the MDB and a large fraction of the MH cases. For some MH cases, however, the b/a values obtained with the two fits are in good agreement, but the c values are not. The reason is that the generalized ellipse is too simple a shape to fit properly the isophotes which have ansae or rectangular-like tips of the bar. In fact, for those cases, the shape enclosed by the isodensities is fatter around the major axis than what the generalized ellipse will allow. Thus the c value obtained by such a fit is not meaningful if the central parts have not been blanked out. This shortcoming was not clear for real galaxies, as there the inner parts are bulge dominated and thus were blanked out.

The upper panels of Fig. 4 show the ellipticity, $1 - b/a$, as a function of semi-major axis a for our three fiducial models. For model MD we present the average of the five times in the time interval [780, 860] for which we have full information on all the particle positions. This was done in order to get a better signal-to-nose ratio, and was possible because the axial ratio does not show any clear evolution with time. This is not the case for models MH and MDB, where evolution is present, and we cannot make averages without losing information. These curves establish quantitatively the general impression we had already from Figs 2 and 3, namely that the bar in model MH is much thinner than that in model MD, the one in MDB being intermediate. Indeed the $(1 - b/a)_{\max}$ is 0.75, 0.44 and 0.69 respectively for models MH, MD and MDB. The run of the ellipticity with radius is also different in the three cases. For model MD the $1 - b/a$ rises to a maximum, occurring around $a = 1.9$, and then drops again. In many cases the drop after the maximum is more gradual than that shown in the figure. This means that the isodensities are nearer to circular in the innermost and outermost parts of the bar and are more elongated in the intermediate region. For models MH and MDB the ellipticity curve is quite flat, meaning that the bar is thin even in the inner and outermost parts. After this flat region there is a very steep drop to a near-circular value. The value of a at which this drop occurs increases noticeably with time, so that making time averages would have smoothed out this feature considerably. Right after the steep drop there is a region with very low values of ellipticity, after which the ellipticity rises again, albeit to a lower

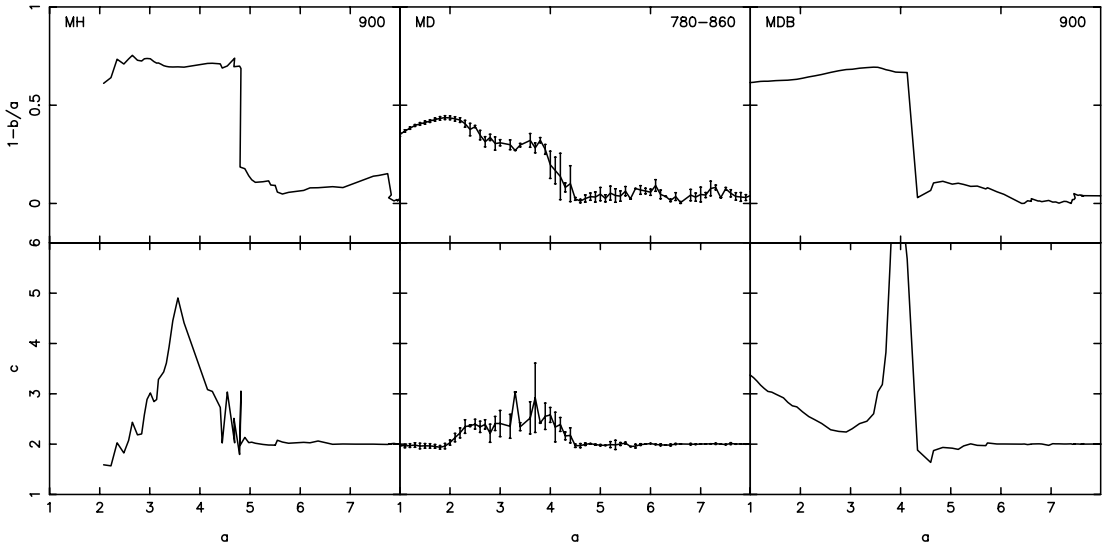

Figure 4. The upper panels show the run of the ellipticity $1 - b/a$ as a function of the semi-major axis a. The lower panels show the run of the shape parameter c, also as a function of a. The left-hand panels corresponds to model MH, the middle ones to model MD and the right-hand ones to model MDB. For reasons explained in the text we show for models MH and MDB the results at a given time, namely $t = 900$, while for model MD we give the average of a time interval, namely [780, 860]. The dispersion during that time is indicated by the error bars. The simulation name is given in the upper left-hand corner and the times in the upper right-hand corner of the upper panels.

value. This intermediate low-ellipticity region corresponds to the near-circular isophotes in the ring region, while the disc outside it has more elongated isophotes, their orientation being perpendicular to the bar, as expected. The disc of models MD and MDB outside the bar region has less elongated isophotes.

The lower panels of Fig. 4 give, for our three fiducial models, the shape parameter c as a function of the semi-major axis a. This is less well determined than the axial ratio. One reason is that the value of c is much more sensitive to noise than the axial ratio, and our isodensities have significant noise as we have 'only' 200 000 particles in the disc. A second reason, as argued above, is that in cases where the shape of the isodensity is not well described by a generalized ellipse, the parameter c is more prone to error than the axial ratio b/a. Although individual profiles can show a number of spurious jumps, due mainly to noise, it is nevertheless possible to see that there are considerable differences between the three fiducial models. The form of this curve for model MD does not evolve with time, so we give here, as in the upper panel, the average of the five times in the time-range [780, 860], in order to increase the signal-to-noise ratio. We note that the value of c increases from a value of around 2 in the centre-most parts to a value of around 3 for $a = 3.3$, and then drops again to a value near 2. This means that the isophotes are well fitted by ellipses in the centre-most and outer parts of the bar, with a region in between with somewhat rectangular-like isophotes. The deviations from the elliptical shape, however, are never very pronounced. The shape of the c profile for model MH is very different. It has a sharp peak in the outer parts of the bar, after which the value of c drops abruptly. The maximum value is very high, around 5, but the region in which high values are seen is rather narrow. The value of a at which the c value drops sharply increases considerably with time, and for this reason we have not taken time averages, but present in Fig. 4 only the values for $t = 900$. For model MDB the fits to generalized ellipses can extend to the innermost regions. Starting from the innermost parts we find first an extended region where c drops from over 3 to roughly 2, and then a very sharp peak of $c = 8.1$ at a radius of 3.9. The drop after the maximum is very steep. For model MDB, as for model MH, the value of a at which the maximum occurs increases with time.

We repeated the exercise for model MDB, this time keeping both the disc and the bulge particles, in order to see what effect the inclusion of the bulge would have on the results. We find that the shape parameter c has considerably smaller values, in fact in between 2 and 3. The ellipticity also drops, by roughly of the order of 0.1. Of course this value will depend on the density profile of the bulge, but the general trend should always be that including the bulge will make the isophotes nearer to ellipses and less eccentric.

The isophotes in the outermost disc region are also of interest, as they are often used by observers to deproject a galaxy, with the assumption that they are circular. In order to check whether this is a reasonable hypothesis, we fitted ellipses to the outermost parts of the disc of our three fiducial models. We find that the deviations of the ellipticity from unity – i.e. of the isodensities from circularity – are less than 0.1 in the outermost parts. For model MH the slight elongation is perpendicular to the bar major axis, while for models MD and MDB it is along it. This may mean that for the latter two we are outside the outer Lindblad resonance, and for the former we are not. We will discuss this further in a future paper, after we have introduced the measurements of the pattern speed. Independent of the orientation of the outermost ellipses, their ellipticity is very near unity. Our fiducial models thus argue that it is reasonable to use the outermost disc isophotes to deproject an observed barred galaxy.

5 DENSITY PROFILES ALONG THE MAJOR AND MINOR AXES OF BARS SEEN FACE-ON

Fig. 5 shows the projected density profiles along the minor and major axes of the bar of our three fiducial simulations at time $t = 700$. We note that the three sets of profiles differ significantly. For MD models the bar has a fast decreasing profile along its major axis, with a slope that is steeper than that of the outer disc. The

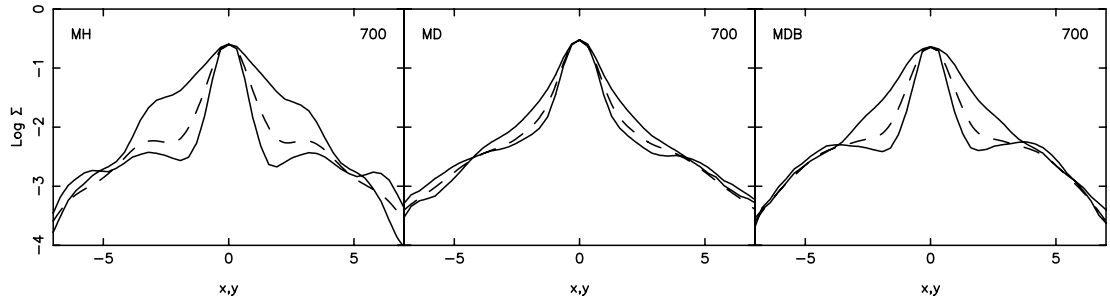

Figure 5. Projected density profiles along the bar major and minor axes (solid lines) and azimuthally averaged (dashed lines). The disc is seen face-on. The left-hand panel corresponds to model MH, the middle one to model MD and the right-hand one to model MDB. The simulation name is given in the upper left-hand corner and the time in the upper right-hand corner of each panel.

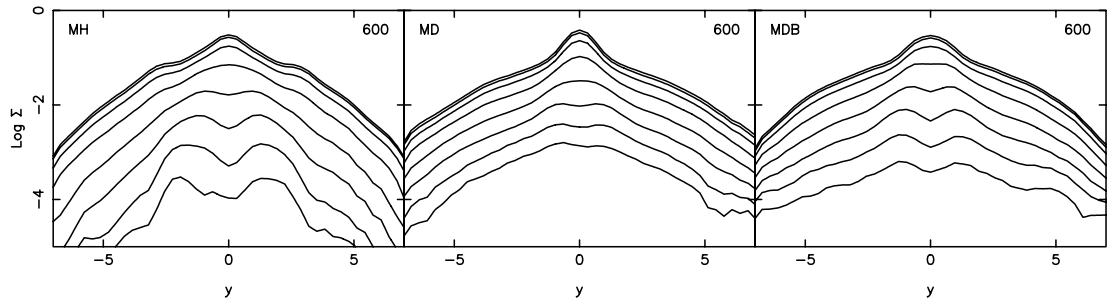

Figure 6. Projected surface density along cuts which are parallel to the major axis (the bar is seen side-on) at equidistant z values differing by $\Delta z = 0.2$. The uppermost curve corresponds to a cut at $z = 0$ and the lower-most one to a cut at $z = 1.4$. The left-hand panel corresponds to model MH, the middle one to model MD and the right-hand one to model MDB, all taken at time 600. The simulation name is given in the upper left-hand corner and the time in the upper right-hand corner of each panel.

MDB major axis profile resembles that of MD. On the other hand, for MH models the profile has a flat part followed by a relatively abrupt drop at the end of the bar region. MD bar profiles stay of the same shape all through the simulation, while the shape of MH profiles shows some evolution; their flatness shows clearest between times 540 and 740.

Model MH also shows a considerable density concentration in the innermost parts, well above the flat part. If such an enhancement was present in observations it would be attributed to a bulge component, and this would have been wrong because we know that this simulation does not have a bulge. It is just an important central concentration of the disc component. It can also be present in models MD and MDB. As, however, the bar has an exponential-like profile, it is not easy to disentangle the contribution of this component from that of the remaining bar. In this respect it is worth noting that the central projected surface density has roughly the same value for the three models.

The minor axis profiles of MD and MH models fall at considerably different rates. This, however, is not a new finding. It is just a result of the fact that the MH bars are considerably thinner than the bars of type MD. In fact from the major and minor axis cuts alone one can get an estimate of the axial ratio of the bar at different isophotal levels, simply by drawing horizontal lines at given isophotal levels on plots like those of Fig. 5 and measuring the radii at which the two profiles reach the given isophotal level.

6 DENSITY PROFILES OF BARS SEEN EDGE-ON

Let us now observe our three fiducial models edge-on with the bar seen side-on, i.e. with the line of sight perpendicular to the major axis of the bar. Fig. 6 shows the projected density along cuts parallel to the major axis made at equidistant z values differing by $\Delta z = 0.2$. Again we note clear differences between the three models. For cuts which are offset from the equatorial plane of the galaxy, model MH shows a clear minimum at the centre, followed on either side by a maximum, followed by a steep drop. This is the direct signature of the peanut, which is due to the minimum thickness in the centre, followed by two maxima on either side. This is very clear in the three cuts which correspond to the highest z displacements, i.e. for z between 1.0 and 1.4. For models MD and MDB, the peanut signature is much less pronounced. The profiles have, if any, a very shallow minimum at the centre followed by a maximum nearer to the centre than in model MH, visible in a rather restricted range of z displacements.

Another clear distinction between the MH and MD models is the form of the profile at $z = 0$. For model MH it shows clear ledges on either side of the peak, while there are no corresponding structures on the MD and MDB profiles. Thus for model MH at time 500 the ledge at $z = 0$ ends roughly at 2.9. These ledges can be found also on cuts somewhat displaced from $z = 0$, but disappear after the displacement has become too large, in this case $|z|$ of the order of 0.4. Similar values are found for time 800. The ratio of the maximum distance to which the ledge on the $z = 0$ cut extends to the radius of the very steep drop found on cuts offset from $z = 0$ is roughly 1.5.

The peak in the centre is due to material that has accumulated in the central regions of the galaxy and is the edge-on analogue of the corresponding density enhancement seen in the face-on profiles. This peak can be seen only on profiles near $z = 0$, and disappears once the displacement from the equatorial plane becomes sufficiently large, i.e. $|z| > 0.8$.

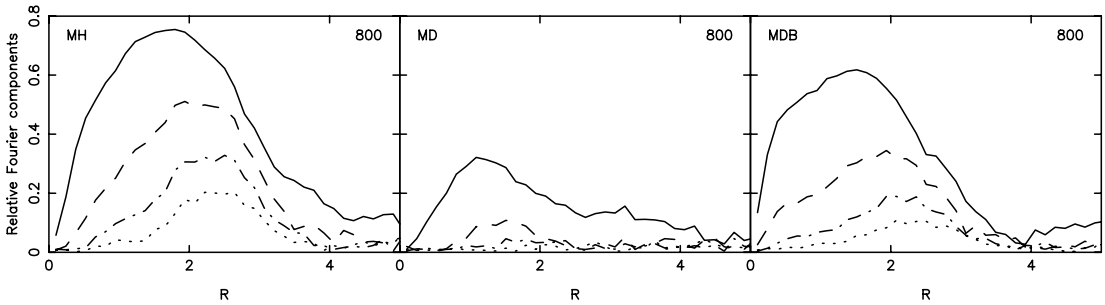

Figure 7. Relative amplitude of the $m = 2$ (solid line), 4 (dashed line), 6 (dot-dashed line) and 8 (dotted line) components of the mass or density. The left-hand panel corresponds to model MH, the middle one to model MD and the right-hand one to model MDB. The simulation number is given in the upper left-hand corner and the time in the upper right-hand corner of each panel.

7 FOURIER COMPONENTS OF THE FACE-ON DENSITY DISTRIBUTION

Fig. 7 shows the relative amplitude of the $m = 2$, 4, 6 and 8 components of the mass or density for our three fiducial cases. To calculate them we first projected the disc particles on the (x, y) plane and then obtained the Fourier components

$$A_m(r) = \frac{1}{\pi}\int_0^{2\pi} \Sigma(r,\theta)\cos(m\theta)\,\mathrm{d}\theta, \quad m = 0, 1, 2, \ldots \tag{6}$$

and

$$B_m(r) = \frac{1}{\pi}\int_0^{2\pi} \Sigma(r,\theta)\sin(m\theta)\,\mathrm{d}\theta, \quad m = 1, 2, \ldots \tag{7}$$

by dividing the surface into annuli of equal width $\Delta r = 0.14$ and calculating the A_m and B_m for each annulus. In practice, instead of the surface density $\Sigma(r,\theta)$ we use the mass, but this comes to the same result because we will be using only the ratios of the amplitudes $\sqrt{A_m^2 + B_m^2}/A_0$.

The maximum amplitude of the $m = 2$ component is biggest in the MH and smallest in the MD model, reflecting the fact that the bar in the MH model is the strongest and that in the MD model is the weakest of the three. Also in model MH the maximum occurs at a larger radius than in MD, and in general the region where this component is large extends to larger radii. This reflects the fact that, as seen in Section 3, the bar in model MH is the longest and that in MD the shortest of the three. The most striking difference, however, between the three models concerns the higher-order terms. Thus for the MD and MDB the $m = 6$ and $m = 8$ components basically stay within the noise, while in the MH model they are 44 and 27 per cent of the $m = 2$, respectively. The relative importance of $m = 4$ is also very different. It is 68, 34 and 55 per cent of the $m = 2$, respectively, in models MH, MD and MDB.

At time 500, the form of the curves is roughly the same as at 800. There is, however, a growth of the relative amplitude with time, which is quite strong for simulations MH, and exists also for MDB. Thus the maximum relative amplitude at time 500 is 0.56, 0.32 and 0.52 for models MH, MD and MDB, respectively. Also the locations of the maxima of simulations MH and MDB move further out with time. At time 500 they are at $R = 1.4$, 1.4 and 1.2, respectively, for the three models. Finally, the secondary maximum occurring in simulation MH at larger radii – R somewhat less than 4 – is very pronounced at time 500 and is located at a smaller radius.

8 LENGTH OF THE BAR

Measuring the length of the bar is not unambiguous and several methods have been proposed so far. In order to apply them to our simulations we have had in certain cases to extend or modify them. Thus we have defined the length of the bar as follows.

(i) From the value of the semi-major axis at which the ellipticity is maximum ($L_{\mathrm{b}/a}$). One can use this value as such, or take a multiple of it. Here we adopted the former.

(ii) From the steep drop in the run of the ellipticity (or axial ratio) as a function of the semi-major axis (L_{drop}). As we saw in Section 4, in model MH the ellipticity presents a steep drop towards the end of the bar region. Although this is not the case for model MD we will still use the radius at which the axial ratio shows the largest drop as a possible measure of the bar length, because it is a straightforward and direct method and it does not introduce any ad hoc constants. It could prove to be a good estimate for cases like model MH, where the drop is clear. It can unfortunately not be used blindly, because in some cases, as in model MD, there may not be a steep drop.

(iii) From the phase of the bar (L_{phase}). The phase of a perfect (theoretical) bar should be constant. This is of course only approximately true in N-body or observed bars. Nevertheless the phase varies little and the bar can be defined as the region within which the phase varies less than a given amount. Instead of considering the differences between the phases in two consecutive annuli, which may be heavily influenced by noise, we use a somewhat less local definition. We first calculate the phase of the $m = 2$ component of the whole disc, i.e. the phase of the bar. Then we repeat the exercise after slicing the disc in circular annuli. In the innermost parts the amplitude of the $m = 2$ is very low and the noise in the phase can therefore be important. Then there is a region where the phase is nearly constant and equal to the phase of the bar, and then it starts varying with radius. We define as length of the bar the radius of the first annulus for which the phase differs by more than arcsin(0.3) from the phase of the bar. The choice of the constant is of course ad hoc. It has simply been estimated so as to give reasonable results in a few test cases.

(iv) From the $m = 2$ component, or from the ratio of the $m = 2$ to the $m = 0$ components ($L_{m=2}$). In a model in which the disc does not respond to the bar, one would expect the end of the bar to be where all components except $m = 0$ go to zero. This is not true in N-body simulations and in real galaxies, where the disc responds to the bar and thus is not perfectly axisymmetric. One can, nevertheless, get an estimate of the bar length from the radius at which the relative $m = 2$ component is less than a given fraction of

Table 1. Length of the bar.

Model	Time	$L_{b/a}$	$L_{\rm drop}$	$L_{\rm phase}$	$L_{m=2}$	$L_{\rm prof}$	$L_{\rm zprof}$	$L_{\rm Agr}$	L_1	L_2	LP_1	LP_2	LP/L_2
MH	540–660	2.9	3.4	4.1	3.4	4.3	2.9	2.6	3.4	3.4	1.7	1.9	0.5
MH	540–660	0.2	0.6	0.8	0.2	0.5	0.2	0.3	0.7	0.7	0.3	0.2	
MD	540–660	2.0	3.5	4.0	4.1	4.6	2.4	2.5	3.3	3.1	1.0	1.1	0.3
MD	540–660	0.1	1.6	1.6	0.2	0.3	0.5	0.2	1.0	1.1	0.1	0.1	
MDB	540–660	2.8	3.4	3.3	3.0	3.3	2.5	2.3	3.0	3.0	1.3	1.4	0.5
MDB	540–660	0.2	0.1	0.1	0.1	0.1	0.2	0.1	0.4	0.5	0.3	0.1	
MH	740–860	2.8	4.4	5.1	4.3	5.5	3.6	2.9	4.1	4.3	2.2	2.5	0.6
MH	740–860	0.2	0.1	0.9	0.4	0.5	0.1	0.1	1.0	1.0	0.0	0.1	
MD	740–860	2.1	4.3	2.4	4.1	4.4	2.1	2.3	3.1	2.7	1.0	1.2	0.4
MD	740–860	0.1	0.2	2.0	0.1	0.3	0.4	0.2	1.1	0.9	0.2	0.0	
MDB	740–860	3.3	3.9	3.7	3.4	3.8	2.9	2.6	3.4	3.4	1.5	1.7	0.5
MDB	740–860	0.1	0.1	0.1	0.1	0.1	0.1	0.1	0.5	0.5	0.1	0.1	

the maximum, provided there is no clear spiral structure. Here we will adopt the radius at which the relative $m = 2$ component reaches 20 per cent of its maximum value as length of the bar. Again the choice of the constant is ad hoc, estimated so as to give reasonable results in a few test cases.

(v) From the face-on profiles ($L_{\rm prof}$). We take the difference between the projected density profiles along the major and minor axes of the bar. This is of course zero at the centre and increases with distance to reach a maximum and then drops. In a theoretical case of a bar in a rigid disc, the end of the bar would be where the two projected density profiles became equal again. Because in *N*-body simulations the disc is responsive, the difference will not be zero even in the disc. We thus define as bar length the outer distance from the centre at which the difference falls to 5 per cent of the maximum. Again the choice of the constant is ad hoc, estimated so as to give reasonable results in a few test cases.

(vi) From the edge-on profiles ($L_{\rm zprof}$). We can define as length of the bar the distance of the end of the ledge on the $z = 0$ cut from the centre of the galaxy.

(vii) From the ratio of the intensities in the bar and the inter-bar region ($L_{\rm Ohta}$ and $L_{\rm Agr}$). Ohta et al. (1990) defined as bar region the zone with a contrast $I_{\rm b}/I_{\rm ib}$ exceeding 2, where $I_{\rm b}$ and $I_{\rm ib}$ are, respectively, the bar and the inter-bar intensities. These can be simply defined as $I_{\rm b} = I_0 + I_2 + I_4 + I_6$ and $I_{\rm ib} = I_0 - I_2 + I_4 - I_6$. This criterion was modified by Aguerri et al. (2000) to delineate the region where $I_{\rm b}/I_{\rm ib} > 0.5[(I_{\rm b}/I_{\rm ib})_{\rm max} - (I_{\rm b}/I_{\rm ib})_{\rm min}] + (I_{\rm b}/I_{\rm ib})_{\rm min}$. The length of the bar is then simply the outer radius at which $I_{\rm b}/I_{\rm ib} = 0.5[(I_{\rm b}/I_{\rm ib})_{\rm max} - (I_{\rm b}/I_{\rm ib})_{\rm min}] + (I_{\rm b}/I_{\rm ib})_{\rm min}$. This definition can be applied to *N*-body bars by changing the intensity for the density, so we will adopt it as one of our definitions. Contrary to other definitions, it has the advantage of being applicable to analytic models for which the length of the bar is known exactly. We have thus applied it to all models in Athanassoula (1992) and found in all cases an agreement of better than 4 per cent, except for the models with the very thin homogeneous bars of axial ratio *a*/*b* larger than 4, where the error can reach 8 per cent.

Several of the above definitions are much easier to apply in *N*-body models than in real galaxies, as in the former we are sure to be in the equatorial plane of the disc, and thus we do not have the considerable uncertainties which a deprojection from the plane of the sky can bring to real galaxies. Most of them have been used in one study or another. Unfortunately they have never been applied all to the same case, so as to allow comparisons. For this reason we have applied them all to all simulations and to all time-steps, and give the results for two times of our three fiducial simulations in Table 1. Because these estimates suffer from the existence of noise, we have used an average over a given time-range. This time-range, however, should be rather small, since the length of the bar increases with time. Thus the σ given in the table is an overestimate of the real uncertainty, since it includes the effect of time evolution. The first column in Table 1 gives the name of the model, the second one the time-range over which the average was taken and columns 3 to 9 give the estimates of the various methods. The second line in each case is similar, but contains the values of the dispersion. For the first two estimates ($L_{b/a}$ and $L_{\rm drop}$) we use the ellipse fitting with the generous blanking (cf. Section 4), because this is more generally applicable. We do not include Ohta's estimate in the Table. For the cases where the ellipticity is almost flat (like MH and MDB) $L_{b/a}$ is not meaningful, while for MD the ellipticity profile does not show a steep drop, so that $L_{\rm drop}$ is not well defined. Generally, the largest values are given by $L_{\rm phase}$ and $L_{\rm prof}$, and the smallest values are given by $L_{b/a}$ and $L_{\rm Agr}$. $L_{\rm drop}$ and $L_{m=2}$ generally give estimates which are intermediate.

It is clear that the differences between the various methods are larger than the dispersions within each method. It is thus of interest to see which method, if any, gives the best results. For this, in Figs 8 and 9 we overlay on the isodensity curves taken at times 600 and 800, respectively, circles with radii the various estimates of the bar length. We note that there is no single method which fares well in all cases. For time 600 the best estimates are $L_{\rm drop}$ and $L_{m=2}$ for MH, $L_{\rm zprof}$ and $L_{\rm Agr}$ for MD, and $L_{b/a}$ and $L_{m=2}$ for MDB. For time 800 the best estimates are $L_{\rm zprof}$ for MH, $L_{\rm phase}$ for MD, and $L_{\rm drop}$, $L_{\rm phase}$ and $L_{\rm prof}$ for MDB.

It is also interesting to see whether the average values represent the length of the bar well or not. Column 10 gives the average of all the estimates (L_1) in the first line and the standard deviation in the second. We also tried a second average (L_2), for which we omitted the entries which were considered unsafe. For this we rely on the applicability of the method to the models and not on whether they give results compatible with the visual estimates of the bar. For cases MH and MDB $L_{b/a}$ is meaningless, because the ellipticity profile is very flat. Similarly, for model MD $L_{\rm drop}$ is unreliable because there is no clear drop in the *b*/*a* profile. For model MD

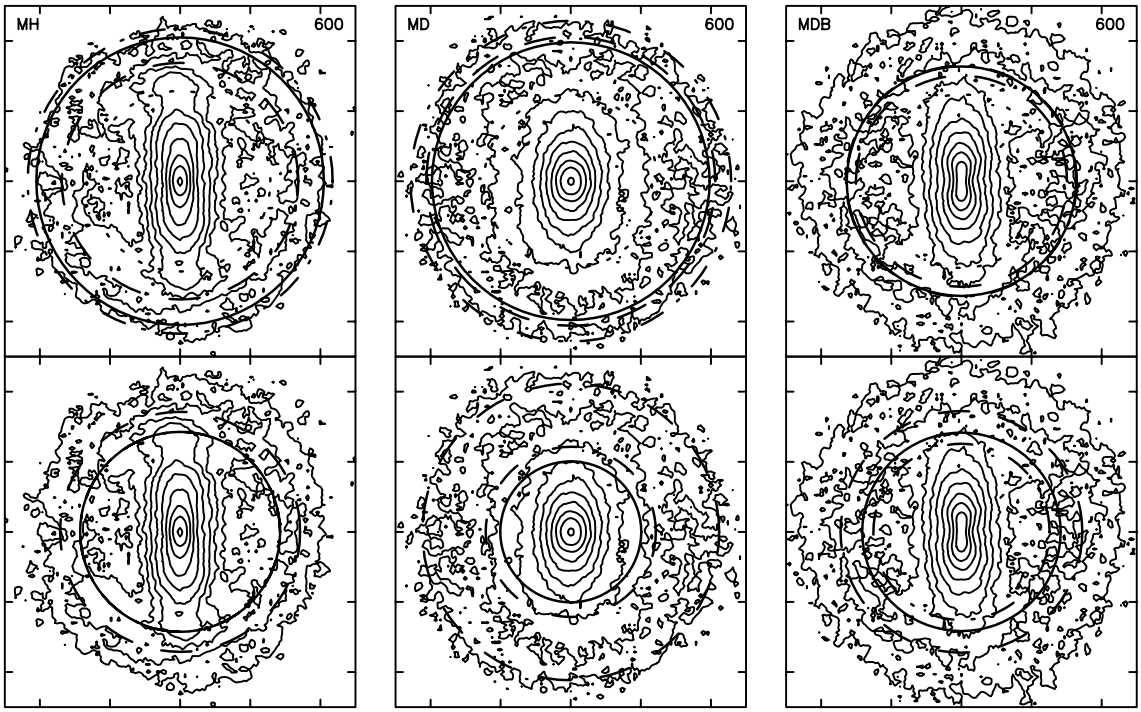

Figure 8. The main determinations of the bar length superposed on isocontours of the projected density for the disc component. In the upper panel we give $L_{\rm phase}$ (solid line), $L_{m=2}$ (dashed), $L_{\rm prof}$ (dash-dotted) and $L_{\rm Agr}$ (dotted). In the lower panel we give $L_{b/a}$ (solid line), $L_{\rm drop}$ (dashed) and $L_{\rm zprof}$ (dash-dotted). The name of the simulation is given in the upper left-hand corner of the upper panels. The isocontours correspond to the time given in the upper right corner. The bar length estimates are obtained by averaging the results of seven times, centred around the time given, and spaced at equal intervals of $\delta t = 20$, as in Table 1. The length between two tick marks is 2 computer units.

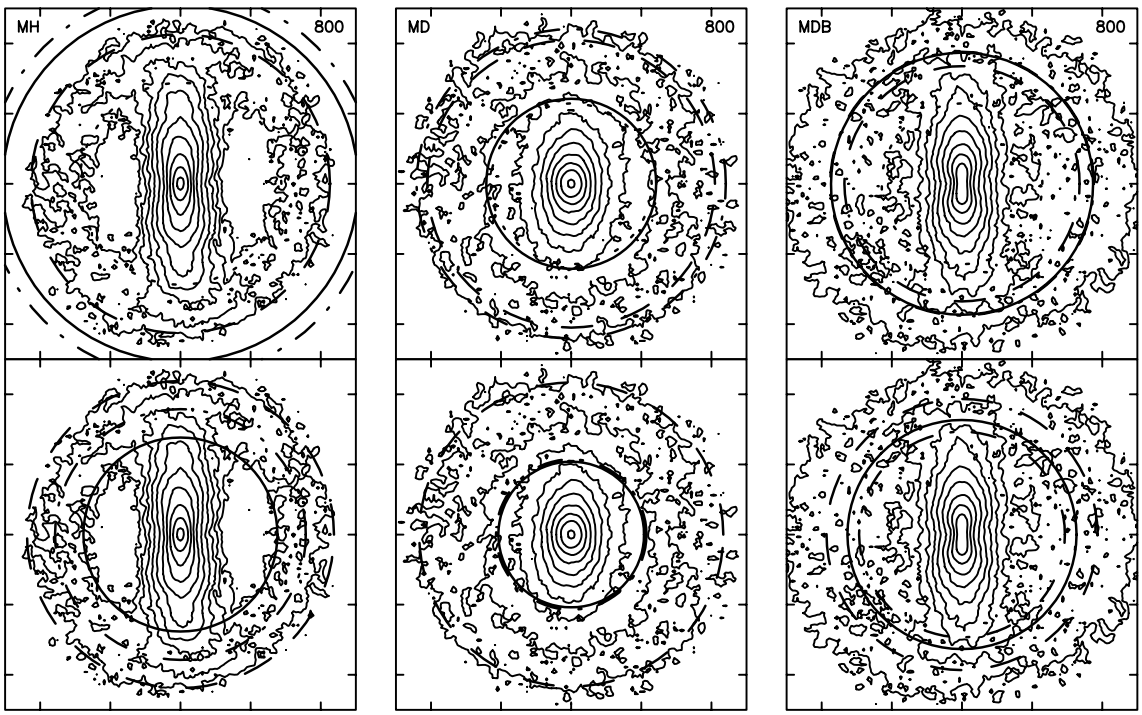

Figure 9. Same as the previous figure, but for time 800.

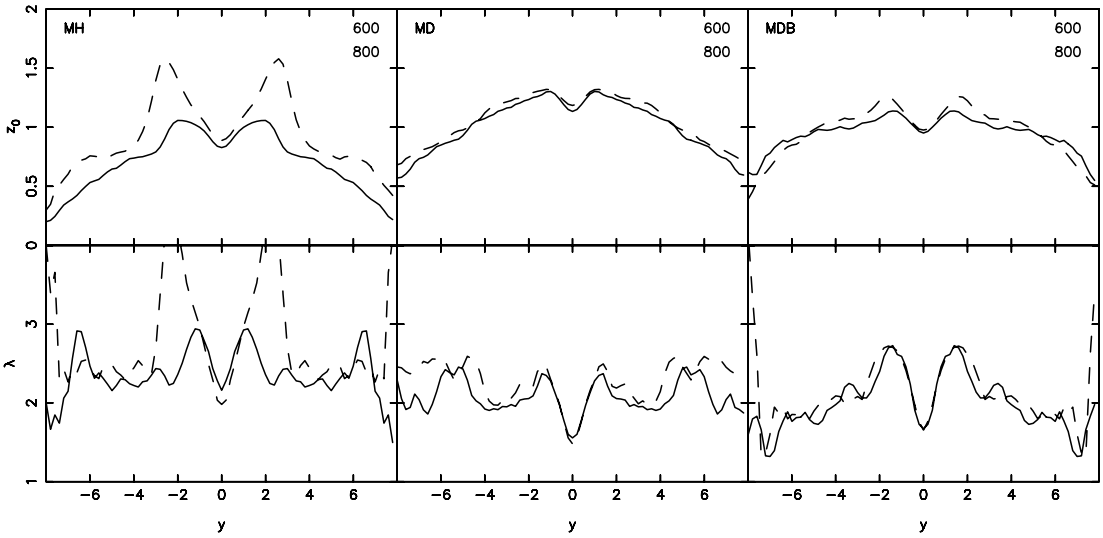

Figure 10. Parameters z_0 (upper panels) and λ (lower panels) of the generalized Gaussian fitting best cuts parallel to the z axis. The left-hand panels correspond to model MH, the middle ones to model MD and the right-hand ones to model MDB. The name of the simulation is given in the upper left-hand corner and the times in the upper right-hand corner of the upper panels. The solid line corresponds to time 600 and the dashed one to time 800.

there are two more estimates that could be unreliable. By examining the individual face-on profiles we see that the difference between the profile along the bar and perpendicular to it is not very dependent on radius (cf. Fig. 5) and thus $L_{\rm prof}$ is badly defined. Finally the ledge is also not clear on the edge-on profiles, so that the $L_{\rm zprof}$ estimate is also unreliable. We thus omitted these two estimates as well for model MD.[3] L_2 and its standard deviation are given in the first and second line of column 11. Taking into account the error bars, we see that average values are good estimates of the length of the bar. This, however, is not a big help, because the error bars are rather large, particularly so for model MD.

Columns 12 to 15 contain information on the peanut length and will be discussed in the next Section.

9 QUANTIFYING THE PEANUT SHAPE

From the third row of panels of Figs 2 and 3 we can see that simulation MDB and the earlier time of simulation MH show a clear peanut shape and simulation MD is boxy, while in the later times simulation MH has a clear 'X' signature. In this Section we will make this comparison more quantitative. We explore two different ways of quantifying the peanut shape.

The first relies on cuts parallel to the major axis when the galaxy is observed side-on, as introduced in Section 6. From such cuts the strength of the peanut can be parametrized by

$$SP_1 = \Sigma_{\rm max}(y, z_{\rm ref})/\Sigma(0, z_{\rm ref}), \quad (8)$$

where y is the distance from the centre along the cut, $z_{\rm ref}$ is the z value at which this cut is made, $\Sigma(y, z_{\rm ref})$ is the projected density along the cut, $\Sigma_{\rm max}$ is the maximum value of the density along the cut and $\Sigma(0, z_{\rm ref})$ is the value at the centre of the cut. The value of SP_1 is heavily dependent on the value of $z_{\rm ref}$. For too low a value of $z_{\rm ref}$, the peanut strength is not well revealed, while for too high a value $\Sigma(0, z_{\rm ref}) = 0$, and therefore the above definition is not applicable. We have chosen $z_{\rm ref} = 1$, which we believe is a reasonable compromise. Such cuts can also tell us the radial size of the peanut, defined as the value of y for which $\Sigma(y, z_{\rm ref})$ is maximum. This also depends on $z_{\rm ref}$. It increases strongly with z for small values of z and less so for larger z values. We choose as our first measure of the peanut length L_{P1}, the value of y for which $\Sigma(y,1)$ is maximum.

Applying this definition to model MH we get $SP_1 = 5.5$ for time 600 and $SP_1 = 12$ for time 800. The corresponding lengths of the peanut are $LP_1 = 1.7$ and $LP_1 = 2.2$ correspondingly. For model MDB we get for SP_1 and time 600 (800) the value of 2.2 (3.0), and for model MD the value 1.5 (1.2). For the latter model the minima and maxima, and therefore the values of the peanut length, are poorly defined, showing that the form is more a box than a peanut.

For the second method we 'observe' our models side-on and make cuts parallel to the z axis at different values of y. For each cut we make a profile of the projected surface density as a function of z. We symmetrize the profiles with respect to $z = 0$, fit to them generalized Gaussians of the form $\exp[-(z/z_0)^\lambda]$ and thus determine the values of z_0 and λ for which the generalized Gaussian fits best the profile. Larger values of z_0 correspond to broader Gaussians, while the parameter λ defines the shape of the generalized Gaussian. For $\lambda = 1$, the generalized ellipse becomes an exponential and for $\lambda = 2$ it becomes a standard Gaussian. For small values of λ the generalized Gaussian is very peaked at the centre and for large ones it has a relatively flat top.

Fig. 10 shows the values of z_0 and λ as a function of the y value at which the cut was made. Because the results are relatively noisy we apply a sliding means. For model MH z_0 shows a clear minimum at $y = 0$ followed by a clear maximum. This is a signature of a peanut. Thus our second way of quantifying the peanut is from the ratio of the maximum of z_0 to its value at the centre, namely

$$SP_2 = z_{0,max}/z_0(0). \quad (9)$$

This is 1.3 (1.8) for times 600 (800) and model MH. For model MD, the value of SP_2 at time 600 (800) is 1.1 (1.1), and for model MDB 1.2 (1.3). From these and a number of other cases we can see that SP_2 can distinguish well between shapes which are boxy,

[3] In fact, the ledge is also difficult to see for model MDB up to time 620. Therefore a more careful treatment would omit this estimate for part of simulation MDB.

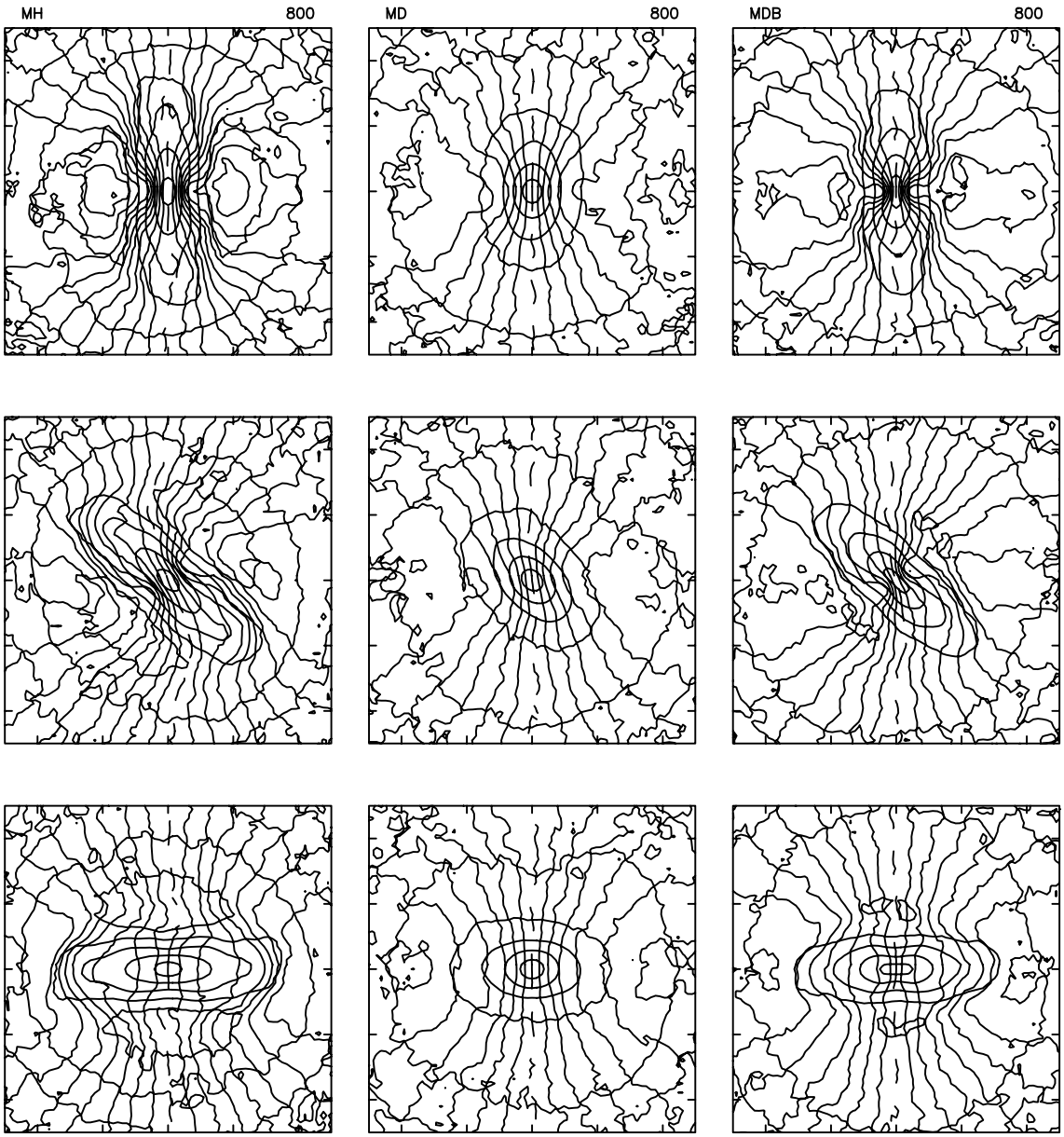

Figure 11. Velocity field of the disc, for three different orientations of the bar: along the y axis (upper panels), at 45° to it (middle panels), and along the x axis (lower panels). The isovelocities are given by thick lines and the kinematic major axis, i.e. the isovelocity corresponding to the systemic velocity (in our case zero), with a dashed line. The Δv between two consecutive isovelocities is 0.1. We also overlay the isodensities with thin line contours. The line of sight is along the y axis. The left-hand panels correspond to model MH, the middle ones to model MD and the right-hand ones to model MDB, all at time 800.

where it gives values hardly above 1, peanuts, where it gives larger values, and 'X' shapes, where it gives considerably larger values. It can thus be used as a measure of the box/peanut/'X' strength.

The location of the maximum of z_0 can be used as a measure of the radial extent of the peanut (LP_2). We find $LP_2 = 2.0$ (2.6) for time 600 (800). The results for the peanut length obtained with the two above definitions averaged in the [540, 660] and [740, 860] time-ranges are listed in columns 13 and 14 of Table 1. The agreement between the two results is of the order of 10 per cent, except for the later time of model MD, where the difference is 20 per cent. We can thus consider either of them, or their average, as a reliable estimate of the peanut length. They show clearly that the radial extent of the peanut increases considerably with time. We also calculated the ratio of the peanut length (as the average of the two estimates) to the bar length (L_2) and give it in the last column of Table 1.

The parameter λ also shows a minimum in the centre surrounded by two maxima, one on either side. This does not necessarily imply that it can be used as a measure of the peanut strength or length. Indeed, the shape of the Gaussians need not correlate with their width.

A different parametrization, based on the a_4 parameter (Bender et al. 1989) often used for elliptical galaxies, will be discussed in a future paper in collaboration with M. Bureau.

10 ROTATION

The orbits of particles in a barred galaxy are far from circular, and

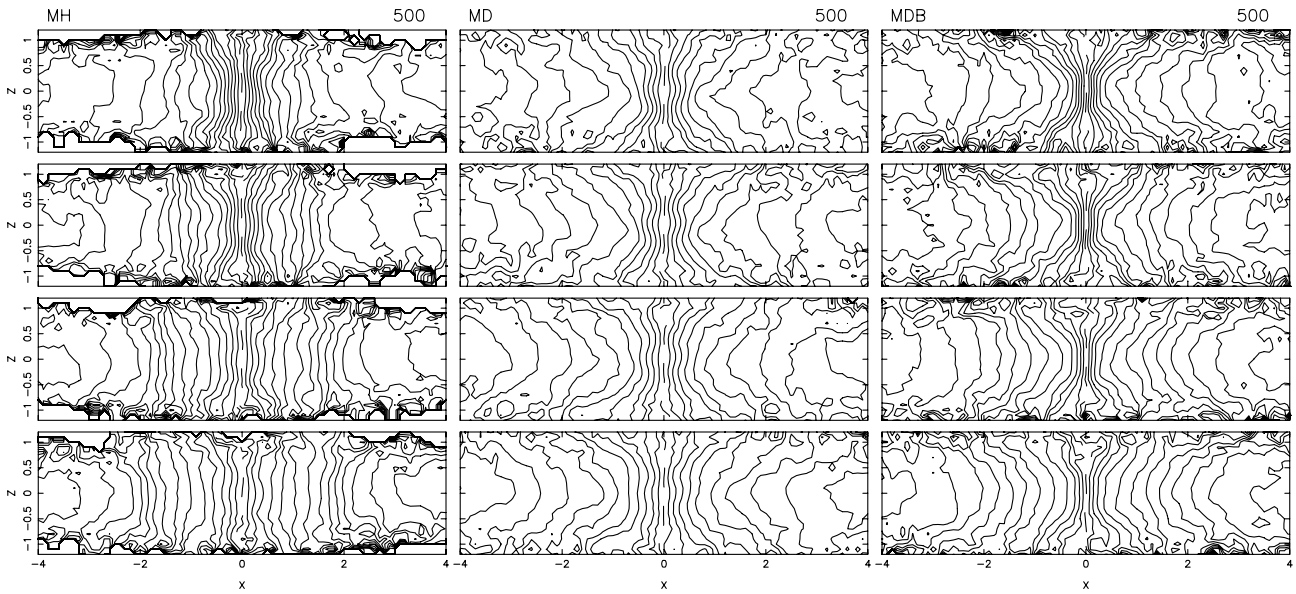

Figure 12. Velocity field of the three fiducial discs seen edge-on, for four different orientations of the bar: end-on (upper row), at 30° to the line of sight (second row), at 60° to the line of sight (third row) and side-on (fourth row). The kinematic major axis is given by a dashed line. The left-hand panels correspond to model MH, the middle ones to model MD and the right-hand ones to model MDB, all at time 500.

this of course reflects itself on the galaxy velocity field. Fig. 11 shows the velocity fields of our three fiducial models. It is obtained in a way that varies somewhat from that of observations, yet it is the most convenient for comparing with observations of galaxies at intermediate inclinations, for which the contribution of the z component of the velocity is relatively small. To obtain it we project all particles on the equatorial plane, observe their v_y velocity component and plot the corresponding isovelocities. For the three views shown in the figure this is equivalent to observing along the bar major axis, at 45° to it and along the bar minor axis, respectively.

Model MD gives velocity fields analogous to those given by previously published models. When we observe along the bar major axis, the isovelocities show a characteristic concentration towards the central region, due to the fact that particle orbits are elongated along the bar and the velocity along an orbit is larger at pericentre than at apocentre. The intermediate angle velocity field shows the *Z* structure characteristic of barred galaxy velocity fields (see e.g. Peterson et al. 1978, for NGC 5383), and finally the velocity field obtained when we view along the bar minor axis shows a sizeable area of solid body rotation in the inner parts.

Several of these features are seen also in the case of model MH, but with some notable differences. Thus when we observe along the bar major axis we note a strong pinching of the isovelocities in the innermost region, on or near the bar minor axis. For the 45 degrees orientation the *Z* shape is much more pronounced than in the MD case, which could be expected as the bar in model MH is so much stronger. The greatest surprise, however, comes from the last orientation, where we view the disc along the minor axis of the bar. The innermost solid body rotation part is there, as for model MD. However, as we move away from the kinematical minor axis the isovelocities show a clear wavy pattern, indicating that the mean velocity is lower at the ends of the bar than right above or right below that. This is due to the fact that near the ends of the bar the particles are at their apocentres. The mean velocities in those regions can be further lowered if the corresponding periodic orbits have loops at their apocentres. Athanassoula (1992) discusses such loops, and the regions where they appear in her models correspond roughly to the low-velocity regions discussed here. She also shows that such loops occur mainly in periodic orbits in strong bars, i.e. that such loops are more liable to be found in model MH than in model MD. A more quantitative comparison will have to wait for a complete study of the orbital structure in these models, which should furthermore elucidate the formation and properties of the ansae. Let us also note here that the velocity field is that of a stellar component and should not be compared to those obtained by observing the gas or from hydrodynamical simulations.

The velocity field of model MDB is intermediate of those of models MH and MD. This holds both for the *Z* pattern seen in the 45° orientation and the wavy pattern at the ends of the bar when we view along the minor axis of the bar. The central crowding, however, is more important than in models MD and MH. This is due to the extra central concentration of the bulge component.

Let us note in passing that no velocity gradients are seen along the line of sight when that coincides with the major or the minor axis of the bar. Furthermore, hardly any velocity gradient can be seen in the MD and MDB cases, even when the line of sight is at 45° to these axes. Thus the existence of a velocity gradient along the minor axis is not a very good criterion to picking out bars and oval distortions and should be left for cases where only limited information along slits is available. If a 2D velocity field is available one should rather look at whether the kinematical major and minor axes are orthogonal to each other (cf. e.g. Bosma 1981 for a discussion) and at the twists of the isovelocity contours.

Fig. 12 shows the velocity field that is obtained when the disc is seen edge-on, for four different angles of the bar with respect to the line of sight, for models MH, MD and MDB, respectively. Again there are important differences between models MH and MD. For model MH the mean rotation does not depend on the distance z from the equatorial plane in a central region, whose size depends on the orientation of the bar. Perpendicular to the equatorial plane it extends roughly as far as the bar material extends. The distance along the equatorial plane is smallest when the bar is seen end-on and biggest when the bar is seen side-on. In the latter case it

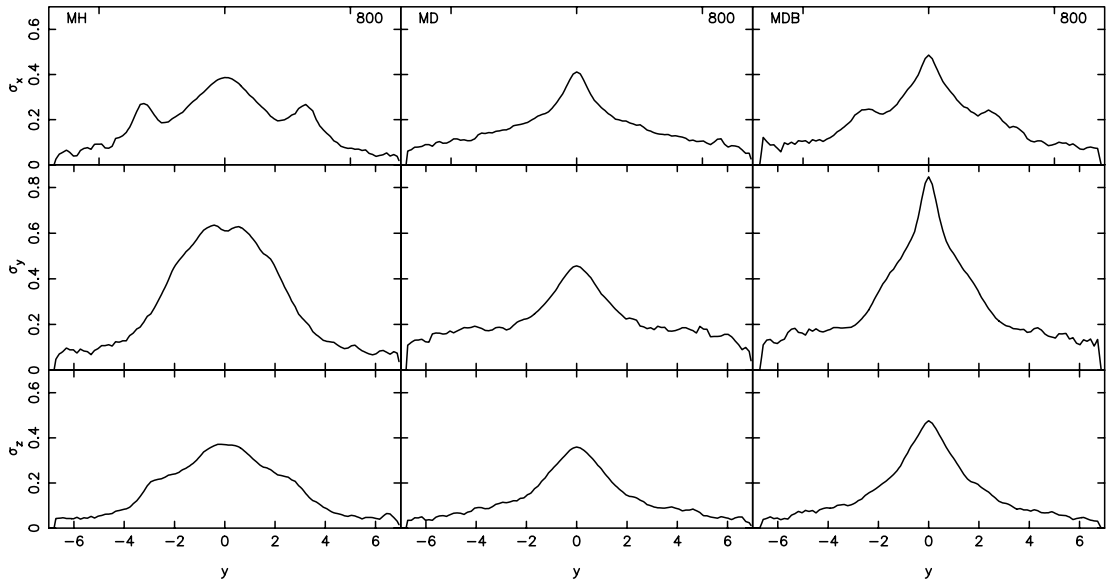

Figure 13. Velocity dispersion as a function of distance from the centre for our three fiducial models at time 800, as discussed in Section 11. The components σ_x, σ_y and σ_z are shown in the upper, middle and lower panels respectively. The left-hand panels corresponds to model MH, the middle ones to model MD and the right-hand ones to model MDB. The simulation name is given in the upper left-hand corner and the time in the upper right-hand corner of the upper panels.

extends over most of the area covered by the peanut. On the other hand in the MD model the mean rotational velocity drops considerably with increasing distance from the equatorial plane, thus again providing a clear dichotomy between the two fiducial cases. Model MDB has a velocity field similar to that of model MD.

As already discussed, the form of the MH bar viewed side-on evolves from box-like to peanut and then to 'X' shaped. When it reaches this last stage the area within which the rotation does not depend on z is somewhat less extended, particularly in the low-density areas on and around the z-axis, on either side of the centre.

11 VELOCITY DISPERSIONS OF A THIN STRIP OF PARTICLES TAKEN ALONG THE BAR MAJOR AXIS

In order to get more information on the motions in our fiducial models we have isolated a strip of particles centred on the bar major axis and having a width of 0.07. Fig. 13 shows the three components of the velocity dispersion, σ_x, σ_y and σ_z, as a function of the distance from the centre of the galaxy measured along the strip, at time 800. The σ_x for model MH shows two sizeable maxima, one at either side of the centre. They should be due to the form of the x_1 orbits in that region, either to the loops that these orbits can have on the major axis, or to their more rectangular like shape, and will be discussed in those terms in a future paper, where the orbital structure of these models will be presented. Here we will note that the shape of the isophotes in that region is very rectangular-like for model MH. The σ_x for model MDB also shows two similar maxima, of relatively lower amplitude. This model also has bar isophotes with a rectangular-like shape, but the maximum rectangularity occurs at larger distances from the centre than the secondary maxima of the σ_x profile. No such maxima can be seen for model MD.

The central value of all three components for model MDB are much larger than those of the other two models, presumably as a result of the presence of the bulge. This is particularly clear for the σ_y component. Also the velocity dispersions are large over a more extended region in model MH than in model MD. This can be easily understood by the fact that the size of the bar is larger, and that the velocity dispersions are larger within the bar region.

It is also worth noting that the σ_y component for model MH has a minimum at the centre, surrounded by two low maxima close to it and on either side of the bar, and followed by a quasi-linear drop. This is not the case for models MD and MDB, where the maximum velocity dispersion is reached at the centre. Again the explanation of this in terms of orbits will be discussed after we present the orbital structure in each model.

12 THE BULGE

We used the inertia tensor to obtain information on the shape of the bulge. For this we first calculated the local density at the position of each bulge particle, using the distance to its six nearest neighbours (Casertano & Hut 1985) and then sorted the bulge particles in order of increasing local density. We believe that the density is more appropriate than the radius, which introduces a circular bias, or than the binding energy, which also introduces such a bias, albeit much less than the radius. We then discarded the 10 per cent in the most dense environment, part of which could be influenced by the softening, and the 10 per cent in the least dense environment, which contains particles at very large distances from the centre, divided the remaining particles into five groups of equal mass and calculated the eigenvalues and eigenvectors of the inertia tensor separately for each group and then for the five groups together. The axial ratios can then be obtained (e.g. Barnes 1992) as those of the homogeneous ellipsoid that has the same moment of inertia. We thus obtain

$$b_b/a_b = \sqrt{q_2/q_1}$$

and

$$c_b/a_b = \sqrt{q_3/q_1},$$

where a_b, b_b and c_b are the lengths of the three principal semi-axes

of the bulge, and q_1, q_2 and q_3 are the eigenvalues of the inertia tensor.

When considered as a whole, the bulge of the fiducial MDB model is an oblate object, with the shortest dimension along the z-axis, i.e. perpendicular to the disc plane. The value of c_b/a_b is around 0.9. However, when we consider each group of particles separately, the departure from sphericity can be much more important. Thus the group with the highest densities, which has a mean distance from the centre of 0.3, is somewhat triaxial with axial ratios roughly 0.75 and 0.7 respectively. The median group, with a mean distance from the centre of 1.2, has axial ratios of roughly 0.9 and 0.8, respectively. In general, as we go from highest to lowest densities, the shape becomes gradually more spherical.

13 SUMMARY AND DISCUSSION

In this paper we present three simulations of bar unstable disc galaxies. Initially in the first model, MH, the halo mass is concentrated in the inner parts, while in the second one, MD, it is the disc mass that dominates in the central parts. The third model, MDB, is similar to model MD, but has also a bulge of mass 60 per cent of the disc mass. In all three cases the halo mass is about five times the mass of the disc. All three models evolve and form a bar in their central parts. The properties of the bar, however, are very different in the three cases.

Model MH forms a very strong bar, which is long and thin when viewed face-on. It is surrounded by a massive inner ring, slightly elongated along the bar. Seen edge-on the galaxy has a peanut or 'X' shape. This model has initially no bulge, so the particles forming the peanut are disc particles, or, more precisely, bar particles. It is thus not appropriate to call this component a bulge, as is often done. This is not, however, the only way that we could have attributed material to a bulge in this bulge-less galaxy. When seen end-on the disc material has a definite central spheroidal concentration, extending well out of the plane, which could easily be mistaken as a bulge sticking out of an edge-on disc galaxy. Surface photometry will only enhance this impression. Projected density profiles, obtained both from face-on and edge-on views, show clear central concentrations in the inner part, which would again easily be attributed to a bulge.

The bar of model MH is not only strong and long, but it is also thin and rectangular-like, as we could show by fitting generalized ellipses to the isophotes. The rectangularity is particularly strong in the outer parts of the bar. Within the main bar region the ellipticity of the bar isophotes does not change much with distance from the centre, and then it drops abruptly to near-circular in the ring region. Outside the ring the isophotes become somewhat more elliptical shaped and are oriented perpendicular to the bar. At sufficiently large distances from the centre they are again near-circular. Thus even in this very strongly barred case the ellipticity of the outer disc isophotes is sufficiently low for observers to be able to consider them circular and use them for deprojecting.

For model MH the projected surface density profiles, obtained from cuts along the bar major axis of the galaxy viewed face-on, show a flat region on either side of the central concentration, the end of which can be used as a measure of the bar length. Similar profiles, now from the galaxy seen edge-on, also show this characteristic ledge. Cuts which are offset from the equatorial plane and parallel to the major axis of the bar reveal a two-horned shape, characteristic of a peanut. They can be used to parametrize the length and the strength of the peanut.

We also Fourier analysed the face-on density distribution of the disc particles. We find that the relative $m = 2$ component is quite large, between 0.6 and 0.8 for the times we discuss here. The position of the maximum is well within the bar; half or a quarter of the way to the centre. Nevertheless, the $m = 2$ component is important all through the bar region. The relative amplitudes of the higher m components are smaller than that of the $m = 2$, but are still very big. Even $m = 8$ is of the order of one third of the $m = 2$. The distance of the location of the maximum of the relative amplitude from the centre increases with m.

The velocity field also shows very strong deviations from circular motion, due to the presence of the bar. When the line of sight is along the bar major axis, or at 45° to it we observe crowding of the isovelocities in the centre-most areas. The 45° orientation shows very clearly the strong Z-type isovelocities, classical of barred galaxies. When the line of sight is along the bar minor axis the isovelocities passing near the ends of the bar show a strong wavy form. This is due to the low mean velocities in the end of the bar region.

When viewed edge-on the model exhibits strong cylindrical rotation over a large area. The bar signature is also clear in the velocity dispersions, which are high in all the bar region. The component perpendicular to the bar major axis shows clear local maxima around the ends of the bar. The component parallel to the bar major axis shows a shallow minimum or a plateau at the centre.

The bar in the MD model is quite different. It is considerably shorter, thicker and less rectangular-like than the MH bar. Viewed edge-on it has a form which is better described as boxy. Its projected density profiles decrease steeply with radius in the bar region and that both in the face-on and edge-on view, as opposed to the flatter profiles of the MH bar. The relative amplitude of the $m = 2$ component is less than 0.4, and the $m = 6$ and 8 components are negligible. The relative $m = 4$ component is considerably smaller than the relative $m = 8$ component of the MH model. Viewed edge-on, model MD does not display cylindrical rotation.

Finally, model MDB has a bar which is intermediate in length and shape to that of the previously discussed two models. Viewed edge-on it has a peanut shape, which never evolves to an 'X' shape, at least within the times considered here. Its projected density profiles, both for the face-on and the edge-on viewing, as well as its velocity field are intermediate of those of models MH and MD. In the face-on profiles there is more difference between the major and the minor axis profiles than in the MD case. On the other hand there is no flat part, except perhaps at the very late times of the evolution, where such a structure starts to form.

In all three cases the formation and evolution of the bar is followed by a substantial inflow of disc material towards the central parts. This implies qualitative changes for model MH. Indeed at the initial times the halo contribution is somewhat larger than the disc one in the inner parts. The halo density distribution does not change much with time, while the disc becomes considerably more centrally concentrated. Thus at latter times the disc dominates within the central region, to a distance larger than an initial disc scalelength. For the MD and MDB spheroids also the density distribution does not change much with time, and again the disc component becomes more centrally concentrated. Thus the central areas become even more disc dominated than they were at the beginning of the simulation. The difference, however, is quantitative, rather than qualitative, as it was for the MH model.

We used a number of different ways of measuring the bar length. Some of them are more suited for MH type models, others for MD types, while others can be used for both. Unfortunately we could not find any criterion which could do well for all simulations and all times. Average values give satisfactory estimates within their

error bars, but their error bars are rather large. This will prove to be a major problem when we will want to compare the length of the bar to the corotation radius, to see how evolution affects this ratio and whether it stays compatible with observational limits (cf. Debattista & Sellwood 2000).

We also introduced two ways of measuring the strength and length of the peanut. They allow to distinguish between boxy, peanut-shaped and 'X'-shaped outlines. They also show that the length of the peanut is considerably shorter than the length of the bar.

ACKNOWLEDGMENTS

We would like to thank A. Bosma for useful discussions and J. C. Lambert for his help with the GRAPE software and the administration of the simulations. We would also like to thank the IGRAP, the Region PACA, the INSU/CNRS and the University of Aix-Marseille I for funds to develop the GRAPE computing facilities used for the simulations discussed in this paper. Part of this paper was written while EA was visiting INAOE. She would like to thank the ECOS-Nord and the ANUIES for financing this trip and INAOE for their kind hospitality.

REFERENCES

Aguerri J. A. L., Muñoz-Tuñón C., Varela A. M., Prieto M., 2000, A&A, 361, 841
Athanassoula E., 1992, MNRAS, 259, 328
Athanassoula E., Morin S., Wozniak H., Puy D., Pierce M., Lombard J., Bosma A., 1990, MNRAS, 245, 130
Athanassoula E., Bosma A., Lambert J. C., Makino J., 1998, MNRAS, 293, 369
Bosma A., 1981, AJ, 86, 1825
Barnes J. E., 1992, ApJ, 393, 484
Bender R., Surma P., Döbereiner S., Möllenhoff C., Madejsky R., 1989, A&A, 217, 35
Casertano S., Hut P., 1985, ApJ, 298, 80
Debattista V. P., Sellwood J. A., 2000, ApJ, 543, 704
Hernquist L., 1993, ApJS, 86, 389
Kawai A., Fukushige T., Taiji M., Makino J., Sugimoto D., 1997, PASJ, 49, 607
Kawai A., Fukushige T., Makino J., Taiji M., 2000, PASJ, 52, 659
Kent S., 1986, AJ, 91, 1301
Kormendy J., 1983, ApJ, 275, 529
Lütticke R., Dettmar R.-J., Pohlen M., 2000, A&A, 362, 435
Ohta K., Hamabe M., Wakamatsu K., 1990, ApJ, 357, 71
Peletier R. F., Balcells M., 1996, AJ, 11, 2238
Peterson C. J., Rubin V. C., Ford W. K., Thonnard W. K., Jr, 1978, ApJ, 219, 31
Toomre A., 1964, ApJ, 139, 1217

APPENDIX A: INITIAL CONDITIONS

In order to generate the initial conditions of our simulations we widely followed the method described by Hernquist (1993), with the following small differences.

(i) For the radial velocity dispersion Hernquist (1993) adopts $\sigma_R^2(R) = C\exp(-R/h)$, where the constant C is normalized so that the Toomre Q parameter (Toomre 1964) has a prescribed value at a given radius. One technical problem with this choice is that the central parts may be very hot, making the epicyclic approximation, on which the calculation of the asymmetric drift and of the azimuthal velocity dispersion is based, totally inadequate. A second problem is that, for certain choices of C and of the reference radius, the disc may turn out to be locally unstable at certain radii. As an alternative we have adopted a Q that is constant all through the disc. This also has some technical problems, but we found them to be less severe than those of Hernquist's choice. Namely in cases with strong bulges one has to take care that the forces are properly calculated in the central parts of the disc before obtaining the epicyclic frequency (see also point iii below). Even so, in difficult cases, it is possible that the streaming velocity becomes larger than the circular velocity. In such cases we artificially lower the value of the streaming velocity to the value of the circular velocity.

(ii) In Hernquist's method, the velocities of the halo particles are drawn from a Gaussian whose second moment is the velocity dispersion of the halo distribution at the radius under consideration. While a Gaussian is the most natural choice, it has the inconvenience of extending to infinity. Thus particles are often drawn with velocities larger than the escape velocity. To avoid this we have used another function, namely:

$$F(v,r) = \begin{cases} C_1\left(1 - \dfrac{v_i^2}{C_2^2}\right) & v_i \le C_2 \\ 0 & v_i > C_2 \end{cases}$$

where v_i is the x, y, or z component of the velocity and the constants C_1 and C_2 are calculated so that the zeroth and second moments are the same as those of the Gaussian. This function limits the values of the velocity components to the interval $(-C_2, C_2)$. While it is still possible for some particles to be drawn with velocities larger than the escape velocity, their number is significantly smaller than in the case of the Gaussian.

(iii) In order to calculate the epicyclic frequency we need first to calculate the force on the disc particles, and for that we used direct summation, including the softening. This allows a more accurate determination of the forces, particularly in the central parts of models with bulges. In fact, Hernquist (1993) does not give sufficient information on how he calculates the force, so we cannot be sure that this is indeed a difference between his method and ours.

APPENDIX B: MEASURING THE MASS, RADIUS AND AXIAL RATIO OF THE RING

We developed two different, independent, methods of fitting a ring and obtaining its basic parameters. In the first we fit a single function $I(R,\theta)$ simultaneously to most of the face of the galaxy. We first exclude the regions with $R < 1$, as they do not contain information relative to the ring, and the regions where $\cos(\Delta\phi) < 0.5$, where $\Delta\phi$ the azimuthal angle measured from the major axis of the bar, because there the ring does not detach itself sufficiently well from the inner part of the profile to allow an accurate fit. To the remaining part we fit a function

$$I(R,\phi) = C_0(\phi)R^{-C_1(\phi)} + C_2(\phi)\exp\{-[R - C_3(\phi)]^2/C_4(\phi)^2\},$$

where $C_i(\phi) = P_{2i} + P_{2i+1}\cos(2\phi)$, $i = 0,\ldots 4$. This is a 10-parameter fit and we call this method and the corresponding fit 'global'.

We also used a different method, inspired from photometric work on barred galaxies. We first obtained a face-on projected density of the model and then made 100 radial cuts with an angle of 3.6° between two consecutive cuts. For each cut we make a two-component fit of the radial density profile using the

functional form

$$I(R,\phi) = D_0 R^{-D_1} + D_2 \exp\{-[(R-D_3)/D_4]^2\},$$

D_0, D_1, D_2, D_3 and D_4 are constants and are determined independently for each radial cut, i.e. for each value of the azimuthal angle. When doing these fits we do not take into account the regions with $R < 1$, as these are too near the centre to contain any useful information about the ring. Because this method deals with each radial cut independent of all the others we call it 'local'.

We thus have for each radial cut a set of D_i values, $i = 0, \ldots, 4$. We now discard those cuts – and the corresponding values of D_i – which are at angles less than 30° from the major axis of the bar, as well as all other cuts where the ring contribution does not detach itself from the background. To the remaining values of (D_i,ϕ) we then fit the simple forms

$$D_\mathrm{i}(\phi) = p_\mathrm{i} + q_\mathrm{i}\cos(2\phi), \quad i = 0, \ldots, 4 \tag{B1}$$

where p_i and q_i are constants.

In the above two methods we have parametrized all the density except for the ring by a simple power law. It could be argued that it would have been more realistic had we used an exponential disc plus a functional form to describe the bar. This, however, would have implied a very large number of free parameters and made the problem badly determined. We find that in most cases a Gaussian profile gives a very good fit to the ring component, while the power law profile is adequate for the remaining part. In this way we limit the number of free parameters. In a large number of cases we checked by eye that the results are satisfactory. As a further measure of the quality of the fits we could compare how well the estimates given independently by the two methods agree. In general we find that the radius of the ring is very well determined. This is less so for its width and mass, as they can be considerably influenced by the wings of the Gaussian. This is not too serious for narrow rings, but much more so for wide ones.

This paper has been typeset from a TEX/LATEX file prepared by the author.